Materials International
Open Access Journal (ISSN: 2668-5728)

Review
Volume 6, Issue 3, 2024, 21
https://doi.org/10.33263/Materials63.021

A Numerical Simulation Approach Towards Efficient $MASnI_3$-Based Solar Cell Using $Mg_2Mn_3O_8$ as the Hole Transport Layer

Mojoyinola Kofoworola Awodele [1], Olusola Akinrinola [1,*], Samson Akinsanmi Ige [2], George Atilade Àlàgbé [1], Omowunmi Abidemi Akinrinola [1,3], Oluwaseun Adedokun [1], Festus Akintunde Ojeniyi [1], Kazeem Kolawole Oyerinde [2,4], Ayodeji Oladiran Awodugba [1]

[1] Department of Pure and Applied Physics, Ladoke Akintola University of Technology, Nigeria; mkawodele@lautech.edu.ng (M.K.A.); oakinrinola40@lautech.edu.ng (O.A.); gaalagbe@lautech.edu.ng (G.A.A.); oadedokun@lautech.edu.ng (O.A.); aoawodugba@lautech.edu.ng (A.O.A.);
[2] Department of Material Science and Engineering, University of Arizona, Tucson, USA; akinsanmiige@arizona.edu (S.A.I.);
[3] Electrical Construction Program, New Brunswick Community College, Saint John, Canada; oakinrinola01@mynbcc.ca (O.A.A.);
[4] Department of Chemical Engineering, Ladoke Akintola University of Technology, Nigeria; oyerindekazeem69@gmail.com (K.K.O.);
* Correspondence: oakinrinola40@lautech.edu.ng (S.A);

Scopus Author ID 57195735050
Received: 11.02.2024; Accepted: 12.05.2024; Published: 10.09.2024

Abstract: Improved material characteristics and associated designs can significantly boost a solar cell's conversion efficiency. A numerical solution to the performance of $MASnI_3$ (MATI) perovskite solar cells was deployed using a solar cell capacitance simulator (SCAPS -1D). The hole transporting layer (HTL) used is magnesium manganese oxide ($Mg_2Mn_3O_8$-MMO). In contrast, titanium dioxide (TiO_2) and fluorine-doped tin oxide (FTO) are used as electron transport layer (ETL) and transparent conductive oxide (TCO), respectively. All these four materials were exploited in the planar configuration of a perovskite solar cell. S1 (FTO/TiO_2/MATI/MMO) gave a power conversion efficiency (PCE) of 27.05%; S2 (FTO/TiO_2/MMO/MATI), S3 (FTO/TiO_2/MMO/MATI/MMO) and S4 (FTO/TiO_2/MATI/MMO/MATI) gave PCE of 24.78%, 27.00% and 27.60% respectively. Optoelectronic optimization was studied on S1 because it shows better stability on the Nyquist plot than others. The intrinsic characteristics of the device's functionality, including defect density, carrier mobility, donor density, and acceptor density, were investigated. The electron affinities of both ETL and HTL were varied within limits, and at a point on the HTL, the efficiency was pushed beyond 52%.

Keywords: numerical solution; perovskite; stability; intrinsic characteristics; carrier mobility; optoelectronic optimization.

1. Introduction

The development of clean, renewable energy sources has become integral to modern scientific and technological efforts to address the world's environmental concerns [1-3], such as affordable and clean energy (Sustainable Development Goal (SDG) 7). One of the essential responsibilities entrusted to modern science and technology in the twenty-first century is the

advancement of clean energy resources as a substitution for conventional energy [4-6] to combat climate change and its impact (SDG 13). One of the practical answers to the global energy supply dilemma is utilizing sunlight's power to generate electricity [5,7]. However, the device (solar cell) must be economical and dependable to compete with traditional sources. Various solar devices have been introduced and studied, including wafer, thin-film, and organic, and found to be highly reliable, cost-effective, and efficient [8]. The use of less material and an increase in energy conversion efficiency are examples of cost-effectiveness [1-8]. While wafer technology can achieve high efficiency, thin film can achieve the same aim with less material [9]. Many materials such as Si, Ge, CIGS, CdTe, CZTS/S, and other inorganic materials are being investigated singly or in combination with other materials in whatever architecture deemed fit [10-14]. Searching for additional materials for the goodness of solar energy, the first perovskite solar cell (PSC) was created in 2009 with a power conversion efficiency (PCE) in order of 4% [1]. Since this period, efforts have tripled over the years to beat the Shockley-Queisser (S.Q.) limit of a single junction solar cell [2-6]. In the efforts to improve the PCE, many material combinations have been proposed and used [8,12]. Perovskite materials can be sandwiched between two materials of different extrinsic orientations, where one serves as the electron transport layer (ETL) and the other hole transport layer (HTL) [8,9]. ETL and HTL are n-type and p-type semiconducting materials, respectively. Materials such as TiO_2, ITO, ZnO, ZrO_2, NiO_2, SiO_2, and SnO_2 and its nanocore shell nanoparticles such as Al_2O_3/ZnO, WO_3/TiO_2, and TiO_2/MgO had been employed as ETLs with PCEs above 20% had been achieved [7-9,12-16]. These materials were preferred because of charge retardation for PCE enhancement [1,8,15-18]. Some PSCs used organic materials such as P3HT and PCMB as HTL [15]. The PSCs quality depends on ETL, HTL, quality of the perovskite thin film, interface layers of the materials, and the ability of transparent conductive oxide (TCO) [19-24].

While some of the perovskite's mysterious features are incredibly desirable, others are causing problems with practical applications of the new technology [25-27]. For example, while perovskite's defect tolerance contributes to high efficiency, the ion-migration process poses a possible danger to stability [28]. It had been established that an inverted structure for a hybrid perovskite solar cell is superior to a single system with a 28.56% PCE via simulation. The same device experimentally yielded 21.01% PCE [17, 28]. A numerical simulation recently produced a PSC with a PCE of 21.16% [24-26]. A new material, a chalcogenide $BaZr_{0.95}Ti_{0.05}S_3$, was used as a PSC absorber, and a PCE of 18.85% was obtained [25,29]. In this paper, four different planar configurations namely: (i) TCO/ETL/p-type/Perovskite/p-type/Metal, (ii) TCO/ETL/Perovskite/p-type/Perovskite/Metal, (iii) TCO/ETL/p-type/Perovskite/Metal, and (iv) TCO/ETL/Perovskite/p-type/Metal were considered. Also, based on their pedigree in the literature, the following materials were deployed, as shown in Table 1, and their non-toxicity yet highly efficient and stable usage. The choice of this p-type ternary alloy material – $Mg_2Mn_3O_8$ (MMO), is based on its low band gap. The band gap is similar to CIGS at 1.45 eV. Its role in solar cells is yet to be reported at the time of conceptualization of this study. The PSCs configurations are presented in Figure 1.

Table 1. Materials and roles in a typical PSCs device.

Role	Materials	Reference
TCO	FTO	[5,21-24]
ETL	TiO_2	[5,7-10,12]

Role	Materials	Reference
p-type	MMO	New material
Perovskite	$CH_3NH_3SnI_3$ (MATI)	[20-24]
Metal	Au	[5,14]

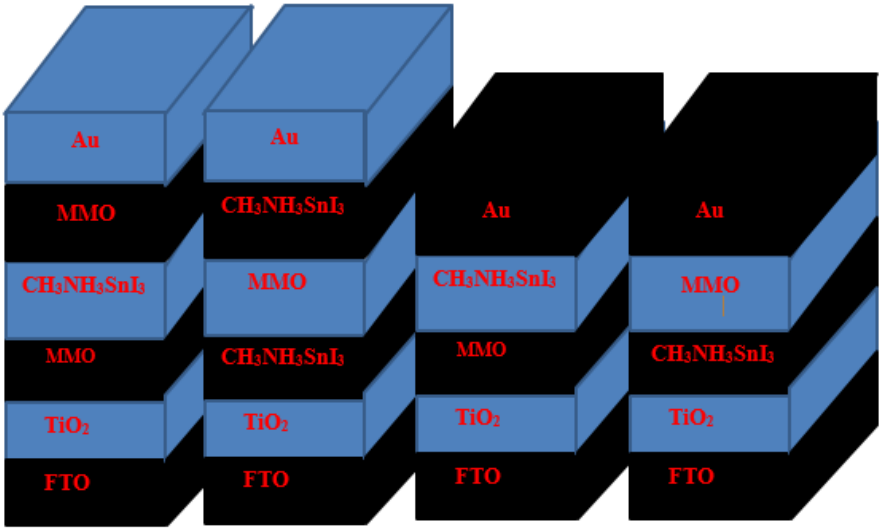

Figure 1. The pictorial of different PSCs architectures (not drawn to scale).

2. Theoretical Considerations

These three equations, Poisson and continuity equations for electrons and holes, are given in Equations 2.1 to 2.3 to be solved by SCAPS-1D as the physics of the device transport, respectively [28-30].

$$\frac{d}{dx}\left[\varepsilon(x)\frac{d\varphi}{dx}\right] = q[p(x) - n(x) + N_D^+(x) - N_A^-(x) + p_t(x) - n_t(x)] \quad (2.1)$$

$$\frac{dJ_n}{dx} = -p\left[G_{op}(x) - R(x)\right] \quad (2.2)$$

$$\frac{dJ_P}{dx} = q\left[G_{op}(x) - R(x)\right] \quad (2.3)$$

where all parameters in the equations are defined as ε is the permittivity, q is the magnitude of the charge of an electron, n for the free electron, $\boldsymbol{p}$ for the free hole, $\boldsymbol{n_t}$ is the trapped electron, $\boldsymbol{p_t}$ is the trapped hole, $\boldsymbol{N_D^+}$ is the ionized donor-like doping concentration, $\boldsymbol{N_A^+}$ is the ionized acceptor-like doping concentration, $\boldsymbol{J_n}$ is the electron current density, and $\boldsymbol{J_p}$ is the hole current density. R is the optical generation rate of recombination due to externally imposed illumination. Numerical methods are employed in solving the above equations because they are coupled and non-linear; despite this, they must hold at every position in the planar model configuration with necessary defined boundary conditions. Also, in transport theory, the electron population may have degenerated (material properties vary with position); thus, $\boldsymbol{J_n}$ and $\boldsymbol{J_p}$ are respectively expressed as;

$$J_n(x) = q\mu_n n\left[\frac{dE_{fn}}{dx}\right] \quad (2.4)$$

$$J_p(x) = q\mu_p n\left[\frac{dE_{fp}}{dx}\right] \quad (2.5)$$

Equations 2.4 and 2.5 are drift equations obtained from band gap, electron affinity, and density of states as a result of electron fields.

3. Device Parameters and Simulations

Many simulation software, such as AMPS, AFORS-HET, Silvaco, SimWindows, and SCAPS-1D, are used to calculate solar cell performances [31]. SCAPS (Solar Cell Capacitance Simulator) is a numerical simulation tool developed and maintained at the University of Gents. It is a general polycrystalline thin-film device simulator. SCAPS-1D solves three coupled PDEs for electrons and hole concentration as a function of positions x. The definition of a new problem in SCAPS is simple; the device can have up to seven layers, and each layer or contact can have its window with all physical and electronic parameters set and changed [32]. The effective states' density and thermal velocity are temperature dependent, although other factors like the bandgap and mobility are temperature independent [33]. As defined in the introduction, configurations i, ii, iii, and iv were labeled S1, S2, S3, and S4, respectively. Opto-electronic parameters used in the simulations were as given in Table 2.

Table 2. Opto-electronics properties of the deployed materials.

Properties	**TiO_2**	**$Mg_2Mn_3O_8$**	**$MASnI_3$**	**FTO**
Thickness (nm)	40	100	200	10
Bandgap(eV)	3.2	1.45	1.3	3.5
Electron Affinity(eV)	4.0	4.1	4.17	4.0
dielectric permittivity (relative)	9	9	6.5	9
CB effective density of states (1/cm^3)	$2x10^{18}$	$1x10^{18}$	$1x10^{18}$	$2x10^{18}$
VB effective density of states (1/cm^3)	$1.8x10^{19}$	$1x10^{19}$	$1x10^{19}$	$1.8x10^{18}$
Electron mobility (cm^2/Vs)	20	50	1.6	20
Hole Mobility (cm^2/Vs)	10	30	1.6	10
Donor density (1/cm3)	$8.41x10^{19}$		0	$2x10^{19}$
Acceptor Density (1/cm3)	0	$8.94x10^{19}$	$7.1x10^{20}$	

Several simulations were conducted via material thickness optimization. The best thickness pair for each material deployed in the device is thus shown in Table 3. The four devices' Nyquist plots and quantum efficiency were also studied [34]. The effects of defect density, interface defect density, donor density, the impact of the optimization of the electron affinity of the ETL and H.T., temperature, and band gap engineering on the PCE of the PSC were also studied.

4. Results and Discussion

The optimized thickness for each material deployed in each device is given in Table 3, and the simulation results of the four devices are presented in Table 4. The optimized thickness of S2 is the least weight among the four devices, with 1.04 µm, while S1, S3, and S4 have 1.44 µm, 1.74 µm, and 2.14 µm respectively. All four devices performed exceptionally well. The best-performed device is the S4, while S1 is the most efficient in terms of materials costs based on the four figures of merit used in the measurement presented in Table 4. The J.V. curve, Nyquist plot, and spectral responses of the four devices are shown in Figure 2. Figure 2(a) shows how the current density varies with the open-circuit voltage in all the devices. S4 has the highest PCE at 27.63%, and S2, the least, has a PCE of 24.78%. It is evident that placing an HTL before the perovskite material will not give a PCE better than putting it just before the back contact, as depicted in S1 and S2 [35]. Also, sandwiching a perovskite between a slice of HTL will not be as efficient as sandwiching the HTL between the perovskite, which eventually yielded a higher V_{OC}, J_{SC}, F.F., and PCE, as

shown in Table 4 [36]. Figure 2(b) shows the admittance measurement via the Nyquist plot. The imaginary part of the impedance density is plotted against the real part. The Nyquist plot is employed in this study to understand each device's stability for better experimental decisions [37]. S1 shows better stability, followed by S3, S4, and S2, the least stable devices. The perovskite solar cell will be more stable if the HTL is placed between the perovskite and the back contact. If sandwiching is necessary, then the HTL should be sandwiched, not the perovskite material, for better stability. Figure 2(c) shows the spectral response of the devices. S2 shows 100% Q.E. up to 580 nm, S1, and S3 show 100% Q.E. above 650 nm, and S4 shows a Q.E. of a little higher than 100% beyond 840 nm. This effect may be due to phonon within the sandwiched MMO for some broad photon wavelengths [38]. The impact of intrinsic optoelectronic parameters on the optimization of such parameters can be explained by the P.N. junction model given in Equation 4.1;

$$I = I_0\left[e^{\left(\frac{qV}{nkT}\right)} - 1\right] - I_L,$$
$$I_0 = aqn_i^2\left[\frac{D_e}{L_eN_A} + \frac{D_h}{L_hN_D}\right], \qquad (4.1)$$
$$V_{OC} = \frac{kT}{q}\ln\left(\frac{I_L}{I_0} + 1\right)$$

Table 3. Optimized the thickness of the materials in each of the devices.

Device	**Configurations (nm)**					
	N		***P***			
	FTO	**TiO_2**	**MATI**	**MMO**	**MATI**	**MMO**
S1	10	30	700	700	-	-
S2	10	30	-	300	700	-
S3	10	30	-	300	700	700
S4	10	30	700	700	700	-

Table 4. The four figures of merit are the measurement of the electrical performance of the devices.

Configurations (p-side)	**V_{OC} (V)**	**J_{SC} (mA/cm^2)**	**FF (%)**	**PCE (%)**
S1 (MATI/MMO)	0.9364	34.3663	84.0567	27.0486
S2 (MMO/MATI)	0.9163	33.9411	79.6810	24.7795
S3 (MMO/MATI/MMO)	0.9379	34.3713	83.7128	26.9857
S4 (MATI/MMO/MATI)	0.9412	34.7784	84.4194	27.6343

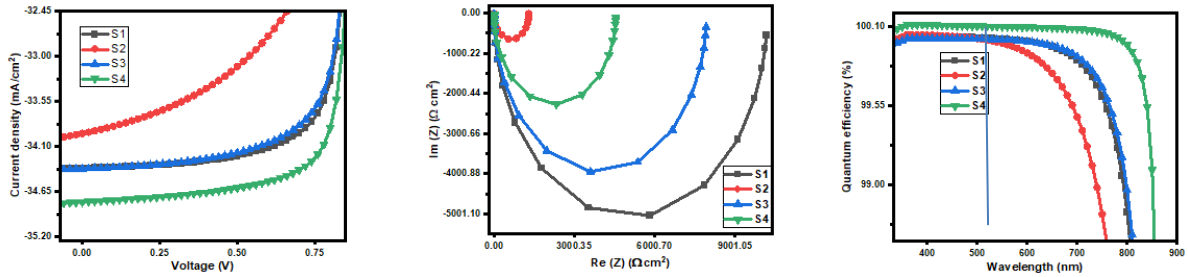

(a) **(b)** **(c)**

Figure 2. Performance pictorial view of the four devices: (**a**) J-V curve; (**b**) Nyquist plot; **(c)** Quantum efficiency measurement.

Table 5. Parameter definition of Equation 4.1.

Parameter	Definition (unit)
I	Current (A)
I_0	Dark saturation current (A)
Q	Electron charge (absolute)
V	Voltage
N	Ideality factor
K	Boltzmann's constant
T	Temperature (K)
I_L	Light generated current
A	The quality factor of the device
n_i	Intrinsic concentration
D_e	Diffusion coefficient of the electron
D_h	Diffusion coefficient of the holes
L_e	Diffusion length for electron
L_h	Diffusion length for holes
$N_{.A.}$	Acceptor doping concentration
N_D	Donor doping concentration
V_{OC}	Open circuit voltage

The parameters in Equation 4.1 are defined in Table 5. These parameters are then optimized within the perovskite to understand its effect on the electrical characterization of the modeled PSCs. The most stable device (S1) is thus optimized for these effects of intrinsic parameters of the perovskite material on the conversion efficiency. The conduction band defect density is varied between 10^{15} cm^{-3} and 10^{21} cm^{-3}, as shown in Figure 3. The V_{OC} and PCE increased as the defect density increased, and the J_{SC} decreased with the defect density boundary F.F. optimized at 10^{20} cm^{-3} while it disappeared afterward. The higher the defect density, the higher the SRH recombination, which lowers the PCE, so it is best to cap the defect density at the optimized value.

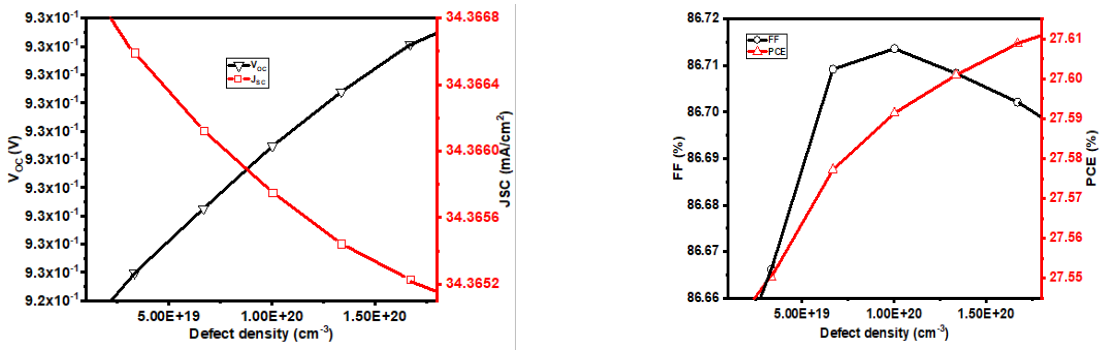

(a) **(b)**

Figure 3. Performance evaluation of the defect density variation in the PSC. (**a**) The plot of Voc and Jsc against Defect density; (**b**) The plot of FF and PCE against Defect density.

The electron mobility varies from 1.6 x 10^{-2} to 1.6 x 10^2 cm^2/Vs.; its effect on the performance is shown in Figure 4. The electron mobility is controlled via doping concentration. The increment in electron mobility reduces the power of the solar cell. The fastest electrons are easily recombined with the holes, which eventually drags the PCE. When the hole mobility is varied within the perovskite, as shown in Figure 5, only the V_{OC} shows constancy while J_{SC}, F.F., and PCE decrease. It may be attributed to band tailing effects caused by the heavy doping of holes

in the material. Only the open circuit voltage would not be affected when perovskite material is heavily doped. High-concentration doping deteriorates the PCE of a PSC.

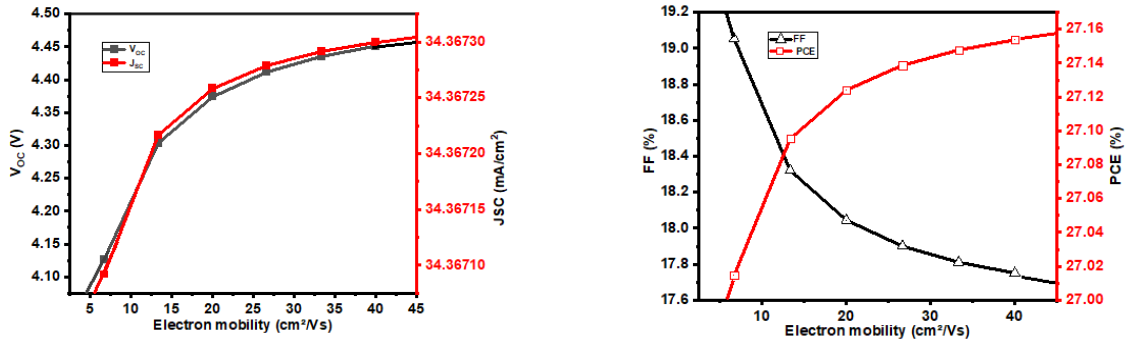

(a) **(b)**

Figure 4. Effect of electron mobility on the performance of the PSC. (**a**) The plot of Voc and Jsc against Electron mobility; (**b**) The plot of FF and PCE against Electron mobility.

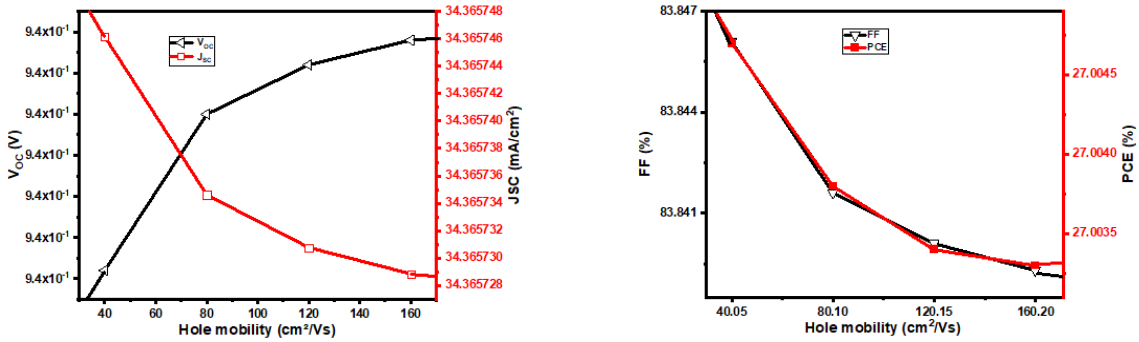

(a) **(b)**

Figure 5. Effect of electron mobility on the performance of the PSC. **(a)** The plot of Voc and Jsc against Hole mobility; **(b)** The plot of FF and PCE against Hole mobility.

The effect of injected donor density from 10^{15} to 10^{19} cm^{-3} in the perovskite material is shown in Figure 6. Generally, the donor density of an absorber in a solar cell is assumed to be nonexistent. The introduction of the donor density negatively affected the performance of the PSC.

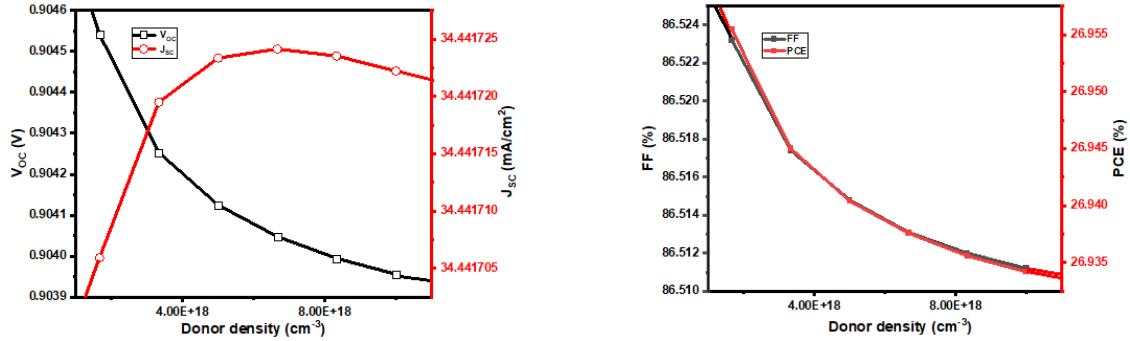

(a) **(b)**

Figure 6. Effect of donor density on the performance of the PSC. **(a)** The plot of Voc and Jsc against Donor density; **(b)** The plot of FF and PCE against Donor density.

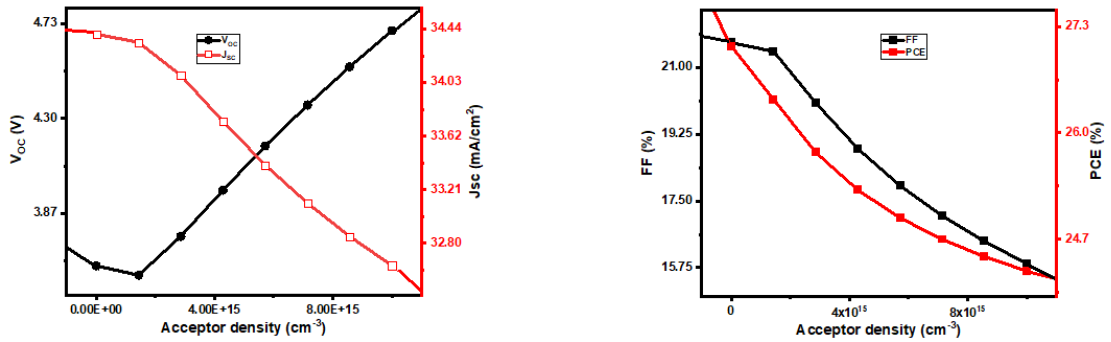

(a) **(b)**

Figure 7. Effect of acceptor density on the performance of the PSC. **(a)** The plot of Voc and Jsc against Acceptor density; **(b)** The plot of FF and PCE against Acceptor density.

The acceptor density was varied from 10^{13} to 10^{16} cm^{-3}; excess doping reduced the performance, as shown in Figure 7. The V_{OC} increased linearly with the acceptor density, while J_{SC}, F.F., and PCE depreciated non-linearly.

The electron affinities for both the ETL and HTL were varied, and their effects on the performance of the PSC were studied. The materials with electron affinity greater than 4.21 are not suitable for use in the solar cell as ETL, as shown in Figure 8. The materials selection based on ETL should be between 3.91 and 4.2 eV. Any choice outside this boundary is not suitable for the solar cell. On the HTL, materials with electron affinities in the range of 2.19 and 3 eV will produce an efficient solar cell, as shown in Figure 9. The simulation revealed a well above 50% PCE for HTL within the range. Simulating the solar cell's performance under ambient temperature is essential—the ambient temperature increases as the sunlight heats the environment. The temperature rise reduces the empirical performance of the PSC. The ambient temperature varied between 280 K to 700 K. The effect of ambient temperature on the solar cell performance is shown in Figure 10. The ambient temperature adversely affected the performance of the PSC. All four figures of merit used to measure performance are greatly affected. The solar cell shows better promise in the area where the ambient temperature can be maintained at nearly 300 K.

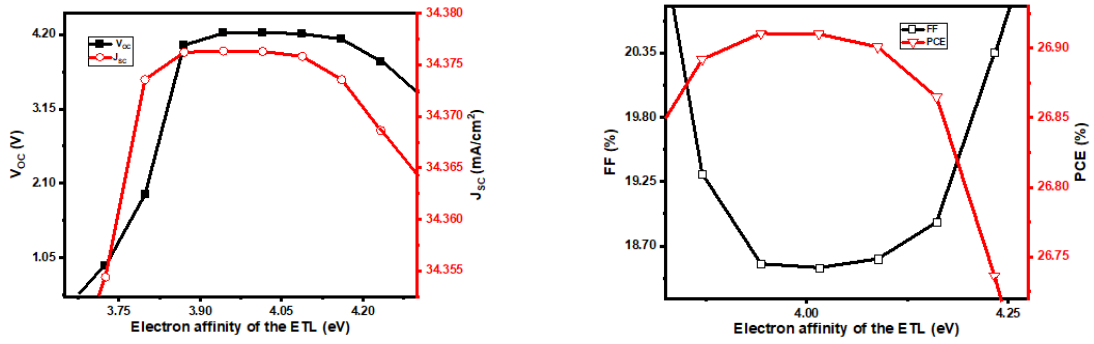

(a) **(b)**

Figure 8. Effect of the electron affinity of the ETL on the performance of the PSC. **(a)** The plot of Voc and Jsc against Acceptor density; **(b)** The plot of FF and PCE against Acceptor density.

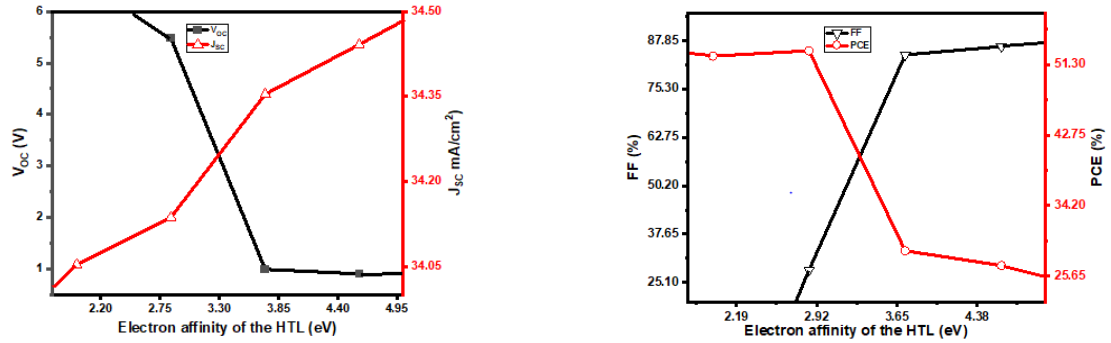

(a) **(b)**

Figure 9. Effect of the electron affinity of the HTL on the performance of the PSC. **(a)** The plot of Voc and Jsc against the Electron affinity of the HTL; **(b)** The plot of FF and PCE against the Electron affinity of the HTL.

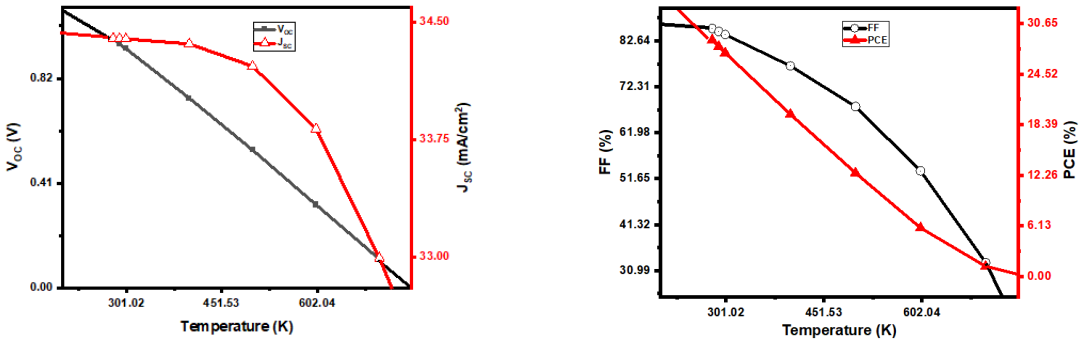

(a) **(b)**

Figure 10. Effect of ambient temperature on the performance of the PSC. **(a)** The plot of Voc and Jsc against Temperature; **(b)** The plot of FF and PCE against Temperature.

The simulation of the band gap variation of the perovskite material while maintaining the thickness and other intrinsic parameters was also investigated. The band gap variation is slower than the performance, as shown in Figure 11. The V_{OC}, FF., and PCE deterioration greatly affected the solar cell's performance. A band gap of 1.7 eV is the least ideal bandgap for absorber deployment in the solar cell. This material will optimally work if its bandgap can be engineered between 1.23 eV and 1.35 eV.

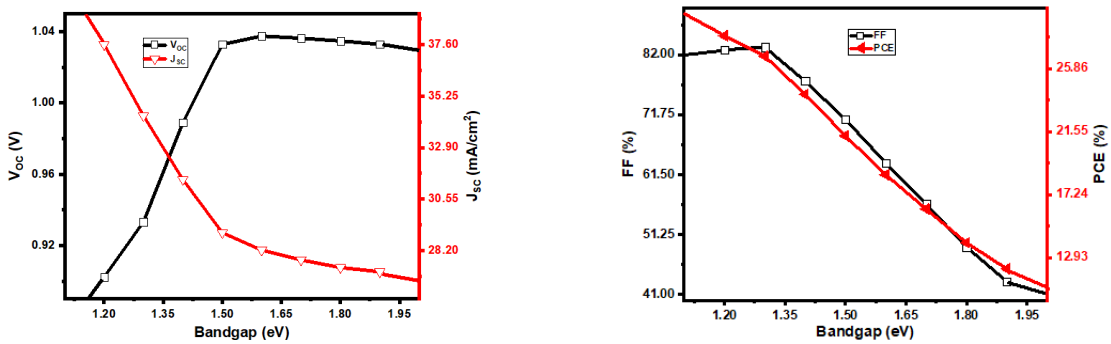

(a) **(b)**

Figure 11. Band gap tuning effect the performance of the solar cell. **(a)** The plot of Voc and Jsc against Bandgap; **(b)** The plot of FF and PCE against Bandgap.

5. Conclusions

Four lead-free perovskites were simulated with MMO as the HTL. We investigated different scenarios of adaptability in its applications. The photovoltaic configurations of (FTO/TiO_2/MATI/MMO) are the most stable, with a PCE of 27.05%. S2 (FTO/TiO_2/MMO/MATI) is the least with 24.8%, S3 (FTO/TiO_2/MMO/MATI/MMO) with PCE of 27%, and S4 (FTO/TiO_2/MATI/MMO/MATI) is the most efficient with 27.6%. In terms of material cost, S2 will be less expensive with a 1.04 µm thickness, while S1, S3, and S4 with a thickness of 1.44 µm, 1.74 µm, and 2.14 µm, respectively, and their material costs are as expressed in that order as well. S1 shows the most favorable terms for PCE, stability, material cost, and weight. It was also observed that adequate tuning on the electron affinity of the HTL between 2.19 eV and 3 eV would improve the PCE to above 52%.

Funding

This research received no external funding.

Acknowledgment

The authors acknowledge Prof. Marc Burgelman (University of Gent, Belgium) for providing free access to the SCAPS-1D simulation software.

Conflicts of Interest

The authors declare no conflict of interest.

References

1. Park, N.-G. Perovskite solar cells: an emerging photovoltaic technology. *Mater. Today* **2015**, *18*, 65-72, https://doi.org/10.1016/j.mattod.2014.07.007.
2. Madurai Elavarasan, R.; Nadarajah, M.; Pugazhendhi, R.; Sinha, A.; Gangatharan, S.; Chiaramonti, D.; Abou Houran, M. The untold subtlety of energy consumption and its influence on policy drive towards Sustainable Development Goal 7. *Appl. Energy* **2023**, *334*, 120698, https://doi.org/10.1016/j.apenergy.2023.120698.
3. Zhao, D.; Cai, J.; Shen, L.; Elshkaki, A.; Liu, J.; Varis, O. Delivery of energy sustainability: Applications of the "STAR" protocol to the Sustainable Development Goal 7 index and its interaction analysis. *J. Clean. Prod.* **2023**, *389*, 135884, https://doi.org/10.1016/j.jclepro.2023.135884.
4. Zanatta, A.R. The *Shockley–Queisser* limit and the conversion efficiency of silicon-based solar cells. *Results Opt.* **2022**, *9*,100320, https://doi.org/10.1016/j.rio.2022.100320.
5. Filho, W.L.; Wall, T.; Salvia, A.L.; Dinis, M.A.P.; Mifsud, M. The central role of climate action in achieving the United Nations' Sustainable Development Goals. *Sci. Rep.* **2023**, *13*, 20582, https://doi.org/10.1038/s41598-023-47746-w.
6. Ehrler, B.; Alarcón-Lladó, E.; Tabernig, S.W.; Veeken, T.; Garnett, E.C.; Polman, A. Photovoltaics Reaching for the Shockley–Queisser Limit. *ACS Energy Lett.* **2020**, *5*, 3029–3033, https://doi.org/10.1021/acsenergylett.0c01790.
7. Kahmann, S.; Loi, M.A. Hot carrier solar cells and the potential of perovskites for breaking the Shockley–Queisser limit. *J. Mater. Chem. C* **2019**, *7*, 2471-2486, https://doi.org/10.1039/C8TC04641G.
8. Roy, P.; Sinha, N.K.; Tiwari, S.; Khare, A. A review on perovskite solar cells: Evolution of architecture, fabrication techniques, commercialization issues, and status. *Solar Energy* **2020**, *198*, 665-688, https://doi.org/10.1016/j.solener.2020.01.080.

9. Nande, A.; Raut, S.; Dhoble, S.J. Chapter 9 - Perovskite solar cells. In Energy Materials, Dhoble, S.J., Kalyani, N.T., Vengadaesvaran, B., Kariem Arof, A., Eds.; Elsevier, **2021**; 249-281, https://doi.org/10.1016/B978-0-12-823710-6.00002-9.
10. Ke, W.; Fang, G.; Wang, J.; Qin, P.; Tao, H.; Lei, H.; Liu, Q.; Dai, X.; Zhao, X. Perovskite Solar Cell with an Efficient TiO_2 Compact Film. *ACS Appl. Mater. Interfaces* **2014**, *6*, 15959-15965, https://doi.org/10.1021/am503728d.
11. Tavakoli, M.M.; Yadav, P.; Tavakoli, R.; Kong, J. Surface Engineering of TiO2 ETL for Highly Efficient and Hysteresis-Less Planar Perovskite Solar Cell (21.4%) with Enhanced Open-Circuit Voltage and Stability. *Adv. Energy Mater.* **2018**, *8*, 1800794, https://doi.org/10.1002/aenm.201800794.
12. Zhao, Z.-W.; Geng, Y.; Troisi, A.; Ma, H. Performance Prediction and Experimental Optimization Assisted by Machine Learning for Organic Photovoltaics. *Adv. Intell. Syst.* **2022**, *4*, 2100261, https://doi.org/10.1002/aisy.202100261.
13. Hu, W.; Yang, S.; Yang, S. Surface modification of TiO_2 for Perovskite Solar Cells. *Trends Chem.* **2020**, *2*, 148-162, https://doi.org/10.1016/j.trechm.2019.11.002.
14. Lu, H.; Tian, W.; Gu, B.; Zhu, Y.; Li, L. TiO_2 Electron Transport Bilayer for Highly Efficient Planar Perovskite Solar Cell. *Small* **2017**, *13*, 1701535, https://doi.org/10.1002/smll.201701535.
15. Chong, K.; Xu, X.; Meng, H.; Xue, J.; Yu, L.; Ma, W.; Peng, Q. Realizing 19.05% Efficiency Polymer Solar Cells by Progressively Improving Charge Extraction and Suppressing Charge Recombination. *Adv. Mater.* **2022**, *34*, 2109516, https://doi.org/10.1002/adma.202109516.
16. Zhang, P.; Wu, J.; Zhang, T.; Wang, Y.; Liu, D.; Chen, H.; Ji, L.; Liu, C.; Ahmad, W.; Chen, Z.D.; Li, S. Perovskite Solar Cells with ZnO Electron-Transporting Materials. *Adv. Mater.* **2018**, *30*, 1703737, https://doi.org/10.1002/adma.201703737.
17. Wang, H.; Cao, S.; Yang, B.; Li, H.; Wang, M.; Hu, X.; Sun, K.; Zang, Z. NH_4Cl-Modified ZnO for High-Performance $CsPbIBr_2$ Perovskite Solar Cells via Low-Temperature Process. *Solar Rrl* **2020**, *4*, 1900363, https://doi.org/10.1002/solr.201900363.
18. Ma, Y.; Hangoma, P.M.; Park, W.I.; Lim, J.-H.; Jung, Y.K.; Jeong, J.H.; Park, S.H.; Kim, K.H. Controlled crystal facet of $MAPbI_3$ perovskite for highly efficient and stable solar cell *via* nucleation modulation. *Nanoscale* **2019**, *11*, 170-177, https://doi.org/10.1039/C8NR08344D.
19. Bisoyi, H.K.; Li, Q. Discotic Liquid Crystals for Self-organizing Photovoltaics. In Nanomaterials for Sustainable Energy, Li, Q., Ed.; Springer International Publishing: Cham, **2016**; 215-252, https://doi.org/10.1007/978-3-319-32023-6_6.
20. Dahal, B.; Li, W. Configuration of Methylammonium Lead Iodide Perovskite Solar Cell and its Effect on the Device's Performance: A Review. *Adv. Mater. Interfaces* **2022**, *9*, 2200042, https://doi.org/10.1002/admi.202200042.
21. Pei, S.; Xiong, X.; Zhong, W.; Xue, X.; Zhang, M.; Hao, T.; Zhang, Y.; Liu, F.; Zhu, L. Highly Efficient Organic Solar Cells Enabled by the Incorporation of a Sulfonated Graphene Doped PEDOT:PSS Interlayer. *ACS Appl. Mater. Interfaces* **2022**, *14*, 34814-34821, https://doi.org/10.1021/acsami.2c10407.
22. Yan, L.; Han, C.; Shi, B.; Zhao, Y.; Zhang, X. Interconnecting layers of different crystalline silicon bottom cells in monolithic perovskite/silicon tandem solar cells. *Superlattices Microstruct.* **2021**, *151*, 106811, https://doi.org/10.1016/j.spmi.2021.106811.
23. Xiao, S.; Qian, W.; Yang, S. Interfaced Structures between Halide Perovskites: From Basics to Construction to Optoelectronic Applications. *Adv. Energy Mater.* **2023**, *13*, 2201472, https://doi.org/10.1002/aenm.202201472.
24. Deeksha; Kour, P.; Ahmed, I.; Sunny; Sharma, S.K.; Yadav, K.; Mishra, Y.K. Transition Metal-based Perovskite Oxides: Emerging Electrocatalysts for Oxygen Evolution Reaction. *ChemCatChem* **2023**, *15*, e202300040, https://doi.org/10.1002/cctc.202300040.
25. Zhang, W.; Huang, L.; Zheng, W.; Zhou, S.; Hu, X.; Zhou, J.; Li, J.; Liang, J.; Ke, W.; Fang, G. Revealing key factors of efficient narrow-bandgap mixed lead-tin perovskite solar cells via numerical simulations and experiments. *Nano Energy* **2022**, *96*, 107078, https://doi.org/10.1016/j.nanoen.2022.107078.
26. Shafi, M.A.; Ullah, H.; Ullah, S.; Khan, L.; Bibi, S.; Soucase, B.M. Numerical Simulation of Lead-Free Sn-Based Perovskite Solar Cell by Using SCAPS-1D. *Eng. Proc.* **2021**, *12*, 92, https://doi.org/10.3390/engproc2021012092.

27. Karthick, S.; Velumani, S.; Bouclé, J. Chalcogenide $BaZrS_3$ perovskite solar cells: A numerical simulation and analysis using SCAPS-1D. *Optical Mater.* **2022**, *126*, 112250, https://doi.org/10.1016/j.optmat.2022.112250.
28. Houmomou, A.M.; Mohammadou, S.; Dzifack Kenfack, G.M.; Tchangnwa Nya, F.; Laref, A.; Mohamadou, A. Toward High-Efficiency CIGS-based Thin-film Solar Cells Incorporating Surface Defects Layer, through a Comparative Study of Electrical Characteristics—SCAPS 1D Modeling. *Energy Technol.* **2023**, *11*, 2201476, https://doi.org/10.1002/ente.202201476.
29. Abdelkadir, A.A.; Sahal, M. Theoretical development of the CZTS thin-film solar cell by SCAPS-1D software based on experimental work. *Mater. Sci. Eng. B* **2023**, *296*, 116710, https://doi.org/10.1016/j.mseb.2023.116710.
30. Parrott, E.S.; Milot, R.L.; Stergiopoulos, T.; Snaith, H.J.; Johnston, M.B.; Herz, L.M. Effect of Structural Phase Transition on Charge-Carrier Lifetimes and Defects in $CH_3NH_3SnI_3$ Perovskite. *J. Phys. Chem. Lett.* **2016**, *7*, 1321-1326, https://doi.org/10.1021/acs.jpclett.6b00322.
31. Shafi, M.A.; Khan, L.; Ullah, S.; Shafi, M.Y.; Bouich, A.; Ullah, H.; Mari, B. Novel compositional engineering for ~26% efficient CZTS-perovskite tandem solar cell. *Optik* **2022**, *253*, 168568, https://doi.org/10.1016/j.ijleo.2022.168568.
32. Gupta, S.; Shishodia, G.; Shishodia, P.K. A comparative study of ZrS_2-based thin film solar cells using the SCAPS solar cell capacitance simulator. *Semicond. Sci. Technol.* **2023**, *38*, 025012, https://doi.org/10.1088/1361-6641/acac4d.
33. Adhikari, A.; Vallejo, O.R.; Diaz, J.E.C.; Martinez-Reyes, J.; Cano, F.J.; Amador, M.d.l.L.O.; Subramaniam, V. A computational study for understanding the effect of various parameters on the performance of three different CI(G)Se-based thin film solar cells. *Opt. Laser Technol.* **2024**, *169*, 110102, https://doi.org/10.1016/j.optlastec.2023.110102.
34. Zhu, R.; Guan, N.; Wang, D.; Bao, Y.; Wu, Z.; Song, L. Review of Defect Passivation for NiO_x-Based Inverted Perovskite Solar Cells. *ACS Appl. Energy Mater.* **2023**, *6*, 2098-2121, https://doi.org/10.1021/acsaem.2c03127.
35. Hossain, M.K.; Bhattarai, S.; Arnab, A.A.; Mohammed, M.K.A.; Pandey, R.; Ali, M.H.; Rahman, M.F.; Islam, M.R.; Samajdar, D.P.; Madan, J.; Bencherif, H.; Dwivedi, D.K.; Amami, M. Harnessing the potential of $CsPbBr_3$-based perovskite solar cells using efficient charge transport materials and global optimization. *RSC Adv.* **2023**, *13*, 21044-21062, https://doi.org/10.1039/D3RA02485G.
36. Du, T.; Qiu, S.; Zhou, X.; Le Corre, V.M.; Wu, M.; Dong, L.; Peng, Z.; Zhao, Y.; Jang, D.; Spiecker, E.; Brabec, C.J.; Egelhaaf, H.-J. Efficient, stable, and fully printed carbon-electrode perovskite solar cells enabled by hole-transporting bilayers. *Joule* **2023**, *7*, 1920-1937, https://doi.org/10.1016/j.joule.2023.06.005.
37. Chowdhury, T.A.; Bin Zafar, M.A.; Sajjad-Ul Islam, M.; Shahinuzzaman, M.; Islam, M.A.; Khandaker, M.U. Stability of perovskite solar cells: issues and prospects. *RSC Adv.* **2023**, *13*, 1787-1810, https://doi.org/10.1039/D2RA05903G.
38. Gao, F.; Wang, X.; Cui, W.-G.; Liu, Y.; Yang, Y.; Sun, W.; Chen, J.; Liu, P.; Pan, H. Topologically Porous Heterostructures for Photo/Photothermal Catalysis of Clean Energy Conversion. *Small Methods* **2023**, *7*, 2201532, https://doi.org/10.1002/smtd.202201532.